C. R. Mecanique 341 (2013) 88–99

Contents lists available at SciVerse ScienceDirect

Comptes Rendus Mecanique

www.sciencedirect.com

Combustion, flow and spray dynamics for aerospace propulsion

Experimental investigation of explosive vaporization of C_6F_{14}

Clélia Desnous [a], Alain Cartellier [a,*], Nicolas Meyers [b]

[a] LEGI-CNRS/Grenoble Université, BP 53, 38041 Grenoble, France
[b] SNECMA Vernon, forêt de Vernon, BP 802, 27298 Vernon, France

ARTICLE INFO

Article history:
Available online 8 January 2013

Keywords:
Flashing
Explosive vaporization
Sudden depressurization
Spray
Superheat
Drop size and velocity
Vaporization flux
PDI
Optical probe

ABSTRACT

Depressurization experiments were conducted with C_6F_{14} for superheats between 5 °C and 90 °C in order to determine how the drop characteristics evolve with the thermodynamic disequilibrium. High-speed imaging indicates that flashing is predominant and leads to very dense sprays. Phase Doppler Interferometer (PDI) was adapted to these optically thick conditions and its ability to provide unbiased velocity and size distributions was carefully checked (even though the flux was underestimated). Experiments show that, for initial superheats above 40 °C, the mean drop velocity linearly increases with the initial superheat while the mean drop diameter remains nearly constant. Such behaviors, not reported in the literature, are tentatively related with a front boiling process in which the drop velocity is driven by the vapor velocity while the drop size is controlled by bubbles exploding at the front. In addition, phase detection optical probes used in combination with PDI data provided number density flux measurements. Global vaporization rates deduced from these local data happen to be fairly consistent with alternate techniques, and the vapor flux exhibits a somewhat weak increase with the superheat.

1. Introduction

Control of the ignition and re-ignition phases is a crucial point in the development of cryogenic rocket engines. Any delay in ignition could lead to an accumulation of combustible in the combustion chamber and thus to a serious over-pressure once combustion begins. This strong rise in pressure can damage the chamber or generate instabilities that could seriously reduce the engine performance. Furthermore, the two-phase nature of the flow within the LOX (liquid oxygen) dome (the feeding cavity upstream of the combustion chamber) can lead to undesirable low frequency hydraulic coupling with the chamber.

The aim of this work is to contribute to the understanding of the LOX jet expansion that occurs as the oxygen ball valve opens and LOX is injected in partial vacuum. The resulting flashing phenomenon concerns the vaporization of a significant proportion of the injected liquid oxygen in some hundreds of milliseconds. This experimental program is part of a larger framework aiming at obtain a database required to validate numerical results of this three-dimensional unstationary flow. Experiments were achieved with a substitution fluid, namely C_6F_{14}, and were focused on the characteristics of the drops created during this sudden depressurization.

Very few data are indeed available in the literature on the size and velocity of drops resulting from flashing and on how these characteristics evolve with the thermodynamic disequilibrium. Brown and York [1] in their study on water concluded that the drop diameter is proportional to the liquid temperature at injection. Most of the later experiments considered

* Corresponding author.
E-mail addresses: clelia.desnous@legi.grenoble-inp.fr (C. Desnous), alain.cartellier@legi.grenoble-inp.fr (A. Cartellier), nicolas.meyers@snecma.fr (N. Meyers).

1631-0721/$ – see front matter
http://dx.doi.org/10.1016/j.crme.2012.10.008

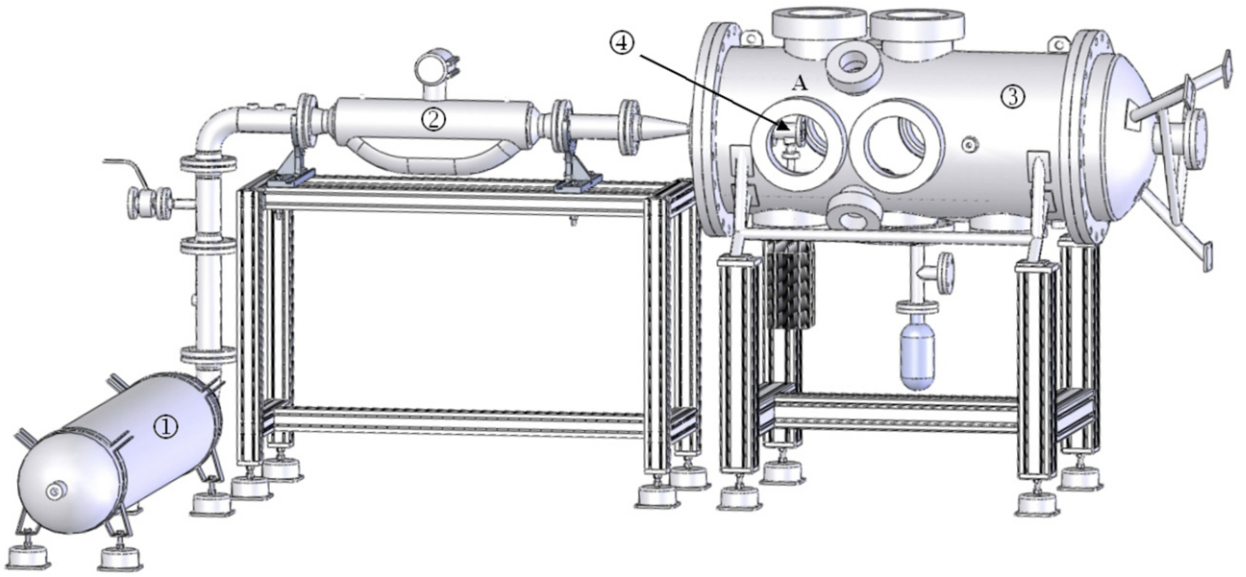

Fig. 1. Flashing experimental set-up. 1. Storage tank. 2. Coriolis mass flowmeter. 3. Vacuum tank. 4. Ball valve.

nozzles and investigated the influence of the liquid flow rate (Hervieu and Veneau [2]). Yildiz et al. [3] observed a decrease of the drop size with the Jakob number, i.e. with the liquid superheat, whatever the liquid initial pressure, nozzle diameter or axial location selected for the measurements. Lecourt, Barricau and Steelant [4] found that the mean drop size and the mean velocity evolve as power laws of a non-dimensional superheat (the later was defined as the ratio between initial liquid superheat and the saturation temperature at the liquid pressure minus the saturation temperature at the vacuum pressure). For a doublet injector, the velocity happened to increase with that non-dimensional superheat (with a 0.43 exponent). The size was found to decrease with that parameter, with a -0.45 exponent for a doublet injector and -0.79 for a swirl injector. Clearly, there is no general agreement about how the drops characteristics evolve with the disequilibrium in presence of flashing. In addition, the prediction of drop flux remains an open issue.

This article will therefore focus on droplet characteristics as measured by a PDI (Phase Doppler Interferometer) in dense sprays arising from flashing and on drop flux measurements using optical probes. In the experiments, a large range of superheats has been considered by varying the initial tank pressure from 1 to 300 mbar. It happens that, almost over all that range, the liquid undergoes explosive boiling as shown by high speed imaging.

2. Experimental set-up

2.1. Flashing set-up

The experimental set-up is shown in Fig. 1. The storage tank pressurized with Nitrogen provides a generating pressure evolving from 1 to 20 bars. A Coriolis mass flowmeter gives access to the instantaneous mass flowrate of FC-72 during the test with a time resolution about 10 ms. Care was taken in filling the circuit to prevent the presence of gas that would invalidate flow rate measurements. The circuit consists then of a tube of internal diameter 25 mm terminated by the main ball valve whose opening time τ_o can be made as small as 30 ms. The distance between the ball and the end of the tube is 28 mm. The valve is installed inside the vacuum tank (capacity 430 liters, pressures from 0 to 11 bars). Various windows provide an optical access for high speed imaging and for PDI measurements.

K-type thermocouples and pressure sensors (Keller PAA23 and PAA25) are installed upstream the main valve to measure the initial storage conditions of the liquid, and also downstream the valve in the vacuum tank. A piston vacuum pump (XtraDry 150) is connected to the depressurization tank and allows a minimum pressure of 1 mbar. A computer controls the valve opening sequence and records temperatures and pressures. It also provides a TTL signal to synchronize additional instruments with the valve opening.

2.2. Control parameters

Due to the difficulties of working with liquid oxygen (LOX) in the laboratory, a substitution fluid was used. Fluorocarbon C_6F_{14} (tetradecafluorohexane), usually named FC-72, was selected to cover the ranges of Jakob and Weber numbers encountered for LOX. The experimental conditions were controlled by four parameters:

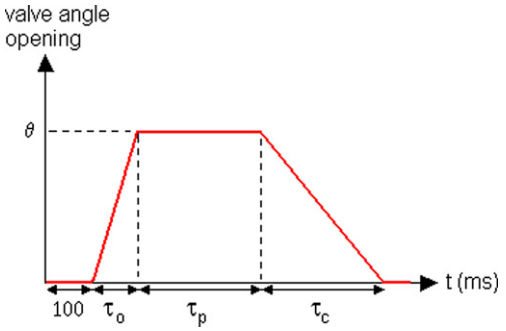

Fig. 2. Valve opening sequence.

(i) The initial superheat, governed by the initial fluid temperature T_{0i} (here the ambient temperature in the laboratory) and the initial pressure in the vacuum tank:

$$\Delta T_i = T_{0i} - T_{sat}(P_{vac,i})$$

where $T_{sat}(P_{vac,i})$ is the saturation temperature of the fluid at the initial vacuum pressure.
The superheat is accounted for by the Jakob number that represents the ratio of sensible heat to latent heat L absorbed (or released) during the phase change process:

$$Ja = \frac{\rho_L c_p \Delta T}{\rho_v L}$$

where ρ_L and ρ_v are the density of the liquid and the vapor respectively, c_p is the liquid specific heat.

(ii) The incoming liquid flux is governed by the liquid generating pressure P_{0i} and by the discharge coefficient for the selected valve opening. The relevant non-dimensional number is a Weber number defined as:

$$We = \frac{\rho_L D U_{inj}^2}{\sigma}$$

where D is the nominal tube diameter (25 mm), σ the surface tension and U_{inj} the mean liquid velocity evaluated at the maximum mass flow rate $Q_{m,\max}$ and for the full tube cross-section. Whatever the vacuum pressure (from 10^{-3} to 0.2 bar), the maximum mass flow rate can be considered as constant for a given generating pressure and a valve opening, the variation in $Q_{m,\max}$ due to the back pressure being at most 9%.

(iii) The valve opening sequence with the choice of the valve angle opening θ, the opening time τ_o, the plateau and closure durations, respectively noted τ_p and τ_c (Fig. 2).
For the ball valve used in these experiments, the fluid begins to flow through the valve only after a 19.6° rotation has occurred. For example, for $\theta = 45°$ and $\tau_o = 100$ ms, the flow starts 44 ms after the beginning of the valve rotation. For $\theta = 45°$, the opening area represents 22% of the full opening area the later corresponding to $\theta = 90°$.

(iv) The contamination of the fluid. The fluid used has constant impurity with about 5 ppm of dissolved oxygen.

The range of superheats covered by the experiments is limited by the minimum vacuum pressure, which is obtained with the vacuum pump at a value of 1 mbar. Therefore the superheats range from 20 °C to 90 °C.

3. Qualitative aspect of the jet

A high speed camera (Phantom V12, 6200 frames/s at a nominal resolution 1280 × 800 pixels) was used to visualize the flashing process. The camera was located in front of window A (Fig. 1), with a spotlight (250 W) for the illumination source on the opposite side of the tank. Recordings were performed with a resolution of 912 × 704 at a frame rate of 7000 frames/s and an exposure time of 10 µs.

Pictures of the jet undergoing flashing are presented in Figs. 3 and 4. Control parameters for the run in Fig. 3 were: $\Delta T_i = 57$ °C ($Ja_i = 340$), $Q_{m,\max} = 1.5$ kg/s ($U_{inj} = 1.8$ m/s), $\theta = 45°$, $\tau_o = 100$ ms, $\tau_p = \tau_c = 500$ ms. In Fig. 4, the only change concerns the initial superheat: $\Delta T_i = 5.5$ °C ($Ja_i = 33$). For both cases, pictures are shown until the maximum angle of the jet is reached.

In Fig. 3, small droplets can be observed during all the expansion of the jet. The angle of the jet quickly increases up to its maximum possible angle, 180°. In Fig. 4, with a superheat ten times smaller, large drops and drop clusters can be seen. The angle of the jet increases much more slowly and the final spray angle is much smaller, around 50°. From these images, a transition between two behaviors seems to take place, namely flashing with an explosive vaporization (the case of Fig. 3) and non-flashing with a much slower vaporization (the case of Fig. 4). Roughly, that transition occurs for a superheat about 10 °C.

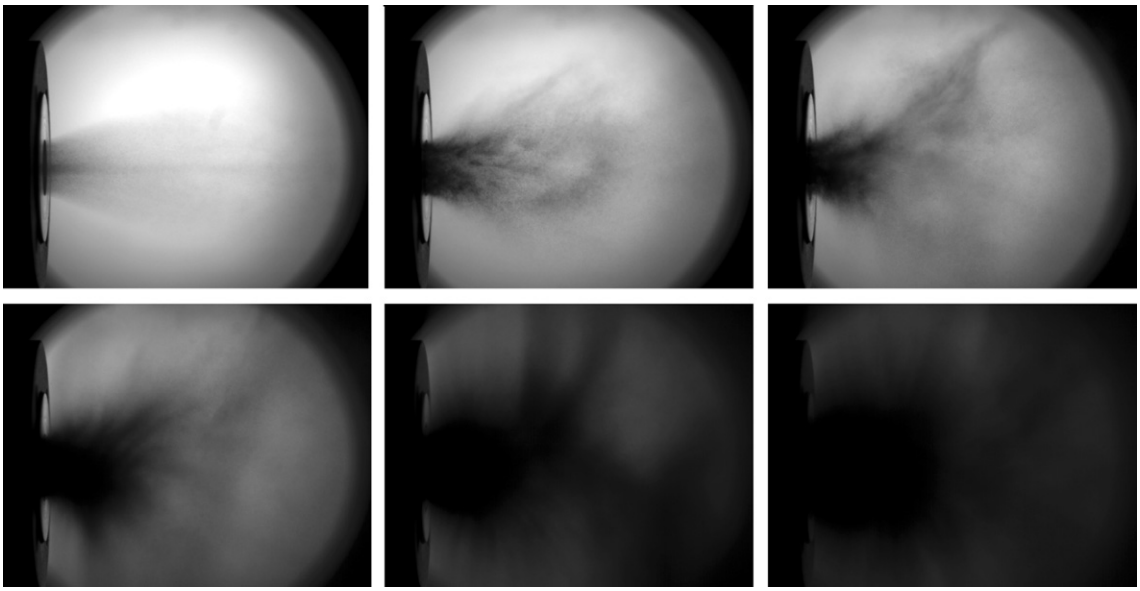

Fig. 3. The first phase of the ball valve opening, from 90 ms to 140 ms (a picture each 10 ms) – $\Delta T_i = 57\,^{\circ}\mathrm{C}$.

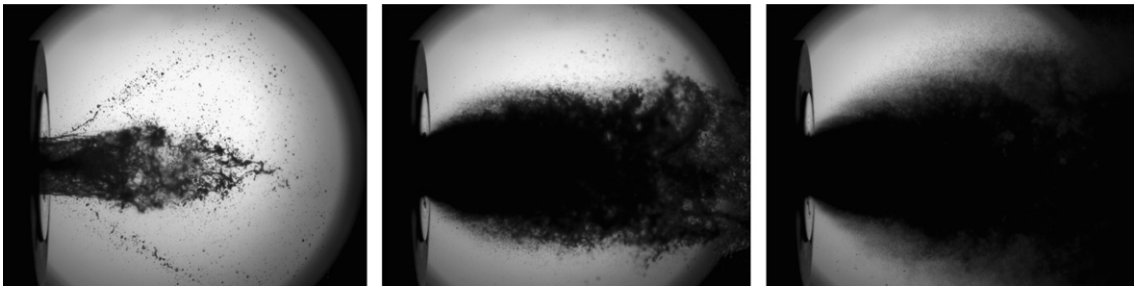

Fig. 4. The first phase of the ball valve opening, from 70 ms to 130 ms (a picture each 30 ms) – $\Delta T_i = 5.5\,^{\circ}\mathrm{C}$.

In the following sections, we report drop size and velocity measurements performed in the flashing regime. Use was made of a Phase Doppler Interferometer (PDI-200 MD from Artium Technologies, Inc., two velocity component system based on two solid state lasers at 473 nm – blue and at 532 nm – green). According to the strong density of the sprays investigated, as illustrated Fig. 3, such measurements are really challenging.

4. PDI measurements in a dense spray

4.1. Principle

This non-intrusive technique can simultaneously measure velocity and size of spherical particles of known refractive index. The technique exploits light scattering by a single particle. To form the probe volume, a laser beam is split into two beams of equal intensity with the Bragg cell, which are then focused by the transmitter lens. Each particle passing through that intersection scatters light. The latter is collected by a receiver and the resulting signal consists of a Doppler burst those high frequency is linearly related with the inclusion velocity projected along the external bisector of the incoming beams. In our system, the probe volume is an ellipsoid with a diameter of 0.32 mm and a length of 5.4 mm. Thanks to a 50 μm slit aperture located in the receiver, the photodetectors only collect scattered light from particles crossing a small region of the probe volume.

For droplets in a gas, the recommended receiver position is at an off-axis angular deviation, the scattering angle, comprised between 30° to 40° away from the optical axis. In this position, the most dominant scattering mode is transmission (refraction) for a refractive index comprised between 1.1 and 3 (cf. scattering mode charts of Naqwi and Menon [5]). When a particle crosses the probe volume, each detector receives a Doppler burst with the same high frequency, proportional to the particle velocity, but with a shift in phase. Knowing the spacing between detectors, the phase shift can be linearly related to the particle diameter. At least two detectors are needed to evaluate the particle size. Three detectors are commonly used in order to extend the size range while maintaining a good resolution. Using three detectors also allows one to diminish the measurement ambiguity and to increase the reliability of size measurements.

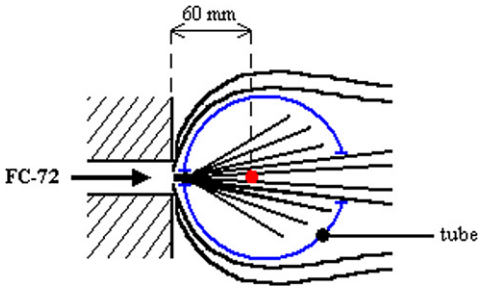

Fig. 5. Position of the measurement location. On the left, the main valve exit and downstream the tube used shield the light propagation.

4.2. Adaptation to the flashing experiment

PDI cannot be used as such in these flashing experiments. Indeed, the jet formed by the sudden depressurization is too dense and optically "thick", and it strongly disturbs both the propagation of the incoming laser beams and that of the scattered light. Some adaptations were thus necessary to gather some exploitable signals.

To ensure, in the present study, clear paths for the beams up to the measurement volume as well as for the light scattered by the drop up to the receiver, a plexiglass tube (17 cm internal diameter) was placed perpendicularly to the jet exit. That tube was also connecting the two facing external windows. Its left wall was located 5 mm downstream the valve exit and a 1 cm diameter hole was facing the jet (Fig. 5). The exit (right side of the tube in Fig. 5) consisted of 7 cm diameter hole. Only droplets passing through the 1 cm diameter hole cross the PDI probe volume. Due to drop inertia, we do not expect any strong distortion in the velocity and size statistics because of this tube. Yet, an influence by way of a change in the vapor velocity distribution cannot be totally ruled out.

Geometrical constraints restrict the possible receiver angular positions with respect to the optical axis. As a first test of this protecting device, the receiver was positioned with its axis perpendicular to the window and we selected a small scattering angle (namely 14°) to optimize the scattered intensity and hence favor the detection of the smallest drops. For a full valve opening, the inner tube happens to be progressively filled with droplets, and the detection frequency was very low. By adapting the valve opening sequence, namely with a partial opening ($\theta = 27°$) and short durations $\tau_o = \tau_p = \tau_c = 100$ ms (Fig. 2), we succeeded to ensure a free optical path for the beams during the whole sequence, and to collect high quality Doppler signals. The data rate, i.e. the number of events detected and validated per second, was quite high, with values evolving from 5 kHz to 30 kHz for an initial superheat varying from 15 °C to 90 °C.

All the measurements discussed in the following have therefore been obtained with the above-mentioned valve opening sequence. Note that only the longitudinal velocity component was measured.

For size measurements, larger scattering angles are required in order to ensure a phase–radius relationship as close as possible to a straight line. This is especially critical for the smallest sizes for which Mie scattering leads to oscillations in the phase–radius relationship. For droplets, the recommended angular deviations are about 30°–40°, since the oscillations in these case are quite small (see Fig. 6, left). Due to geometrical constraints, such large angles were not accessible in the experiment. The maximum possible deviation corresponds instead to a 20.7° scattering angle for measurements performed on the jet axis (Fig. 5). In that case, the receiver optical axis makes a 6.7° angle with the normal to the collecting window.

Let us first discuss the feasibility of size measurements at this angle. Scattering mode charts of Naqwi and Menon [5] show that for scattering angles lower than 30° and for a particle moving in a gas with a refractive index of 1.25, the dominant scattering mode is the same as for scattering angle of 30° or 40°, and correspond to the transmission (refraction) mode. However, for scattering angles lower than 30°, a second scattering mode may become active and thus may alter the quality of the Doppler bursts.

Phase versus diameter diagrams are used to determine the drop diameter. The phase response is linear with the diameter but oscillations centered around the linear response are present for small droplets. For the ideal scattering angle of 40°, there are small oscillations (Fig. 6, left), which correspond to an uncertainty of 0.5% of the full-range of the instrument. In our case, with a 20.7° scattering angle, oscillations are larger (Fig. 6, right), and the uncertainty increases to 2% of the full range. The latter remains quite acceptable: for the optical setting selected, it corresponds to an absolute uncertainty of about 3 μm.

To test further the validity of the 20.7° angular position, we compared the size distributions detected at various angles. First, we performed some measurements at an angle close to the optimum (namely 29.4°) but for a measuring location shifted 2.6 cm above the axis, i.e. somewhat outside the main jet. As part of the droplets entering the shielding tube recalculates in it, the resulting size distribution is expected to be somewhat representative of the actual size distribution in the incoming jet. That "reference" size distribution has then been reported on the linear phase–radius diagrams corresponding to detectors at scattering angles equal to 20.7° (respectively to 14°) in Fig. 7(a) (respectively in Fig. 7(b)). It happens that the unambiguous size measurement range for these two scattering angles (solid lines in Fig. 7) is always wider that the actual size distribution. Both these detectors positions are therefore acceptable for size measurements: they differ by the magnitude of the uncertainty and also by the data rate (as already discussed).

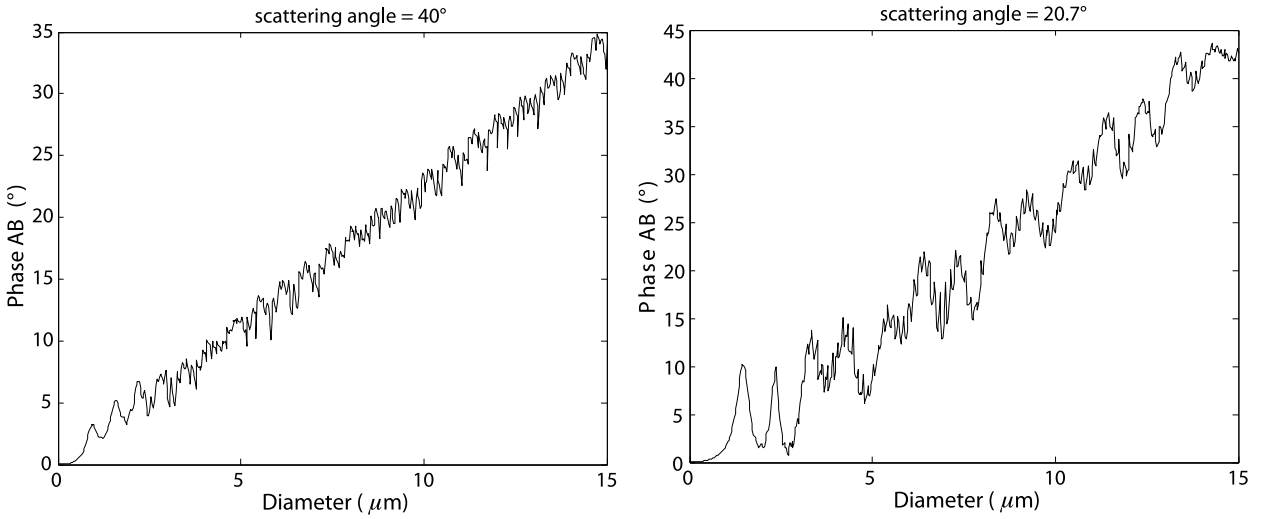

Fig. 6. Oscillations around the linear phase response versus diameter for a scattering angle of 40° (left) and 20.7° (right). Fluid: FC-72, refractive index $n = 1.25$ (Artium Technologies).

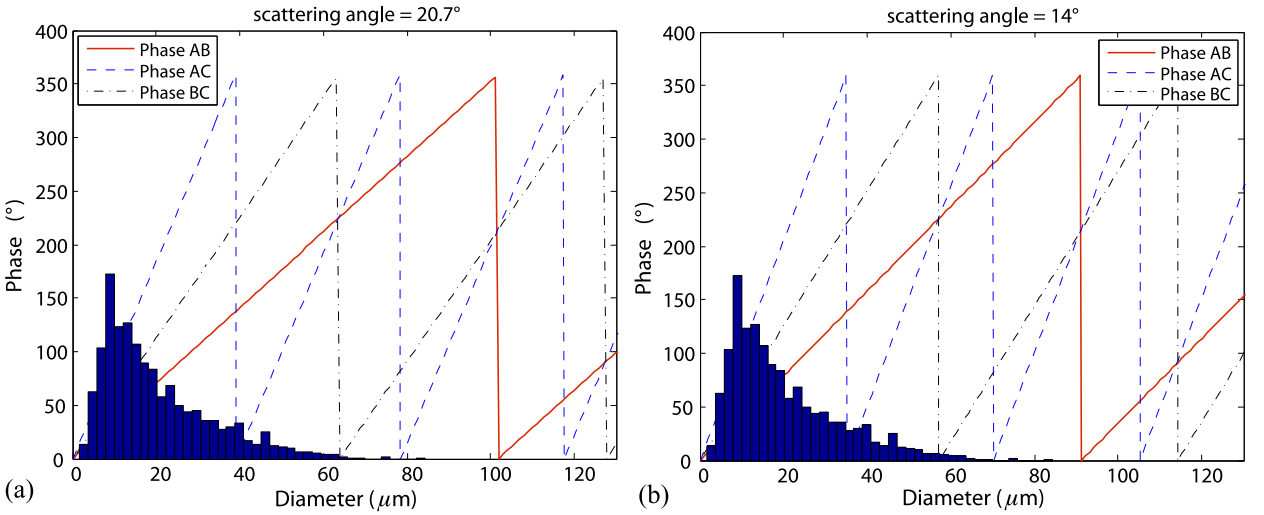

Fig. 7. Phase versus diameter diagram, with a diameter PDF from a run with a scattering angle of 29.4°. Scattering angle: 20.7° (a) and 14° (b).

Second, we compared the size distributions as measured for 29.4° and 20.7° angular positions, and it happens that they are nearly the same. In particular, the arithmetic mean diameters were identical within 1%. This confirms a posteriori that the size distribution obtained away from the jet center is indeed representative of the spray. It also indicates that the smallest drops are correctly detected and that there is no strong bias related with signal amplitude. For completedness, let us mention that size distributions at 14° differ from the others two, probably because of the role of the extra diffusion mode at this low angular deviation.

Third, we compared the velocity distributions detected for 14° and 20.7° angles and these were also nearly identical. The main difference between the 14° and 20.7° angles lies in the detection and the validation rate. The data rate for a scattering angle of 14° (velocity mode only) is about twice as high compared to 20.7° angle.

The above analysis indicates that, for a detector at 20.7°, the velocity and size distributions are indeed reliable and hence representative of the spray. However, many drops are missed by the system and this drawback will affect the flux estimate (see Section 5.3). Therefore, the detection bias happens to be nearly uniform over the entire velocity and size range.

Following this analysis, the detector angular position was set to 20.7°, the others optical settings being given in Table 1, and the diameter measurement range extends from 0.9 to 129.2 μm. In these conditions, we also investigated the influence of the PDI detection parameters, namely the analog threshold, as well as the influence of the validation parameter, namely the Signal-to-Noise Ratio (SNR). SNR, initially set at 0.30, was changed to 0.25 for each detector with all the others parameters maintained constant. No change was observed in the results. The analog threshold sets a minimal value for the voltage threshold level, in order to avoid signal detection on the background noise. Initially, it was set at 100 mV. Runs were

Table 1
Optical settings.

Parameter	Value
Receiver and transmitter focal length	500 mm
Fringe spacing	4.4 µm
Probe volume dimensions:	
ellipsoid diameter	0.32 mm
ellipsoid length	5.4 mm
AB detector separation	21.83 mm
AC detector separation	56.76 mm
BC detector separation	34.84 mm

Table 2
Control parameters and PDI settings for a run with $\Delta T_i = 87\,^{\circ}\mathrm{C}$.

Control parameters		PDI settings	
$P_{0i} = 1.2$ bar		Analog filter = 20 MHz	Burst decimation = 2
$T_{0i} = 19.3\,^{\circ}\mathrm{C}$	$Ja_i = 520$	Mixer frequency = 40.3 MHz	Analog threshold = 100 mV
$P_{vac,i} = 1$ mbar		Sampling rate = 80 MHz	Low SNR 1A/1B/1C = 0.30

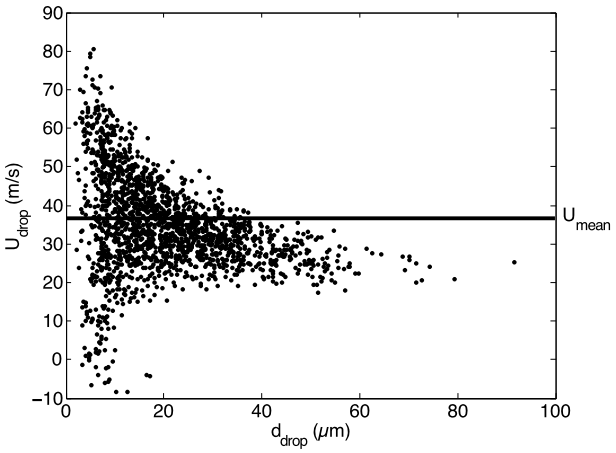

Fig. 8. Velocity versus diameter for a run with $\Delta T_i = 87\,^{\circ}\mathrm{C}$ between 100 and 200 ms.

performed with an analog threshold ranging from 40 mV to 200 mV without showing any drastic change in the velocity and size distributions nor in the data rate.

In the following sections we analyze the droplet characteristics as observed during the plateau of the valve opening sequence, i.e. between 100 ms and 200 ms after the start of the valve opening. Such data correspond to quasi-steady conditions. In particular, thanks to the limited plateau duration, the change in the tank back pressure due to vaporization remains negligible. Actually, the nature of the flow during the opening phase, i.e. the first 100 ms, turns out to be quite complex. In particular, it includes some drops produced by the atomization of liquid films formed on the tube wall. All the results presented were performed at a fixed liquid flow rate (or generating pressure) equal to 0.27 kg/s ($U_{inj} = 0.33$ m/s). The processor electronic settings were adjusted for each run, depending on the initial superheat and the expected maximum velocity.

Table 2 shows the different parameters and initial conditions of a run with an initial superheat of 87 °C. A total of 1797 droplets has been validated during the plateau, with a data rate of 18 kHz. The processor settings correspond to a velocity range from −87.5 to 90.1 m/s.

4.3. Velocity versus size

A typical joint velocity–size plot is illustrated in Fig. 8. It happens that the smallest droplets exhibit a much wider velocity distribution than large ones. Oddly, negative velocities are detected for small drops although the measurements are taken on the jet axis. Such values are tentatively attributed to measurement errors resulting from distorted Doppler bursts. Indeed, the inner tube is progressively filled with droplets during a run. Although their concentration is not large enough to completely block the beams, they may become numerous enough to induce beam deflections that alter the fringe spacing, or to add some extra light scattering contribution to the signals. As we have no definitive explanation concerning the origin of such odd measurements, the data collected will be exploited without any filtering.

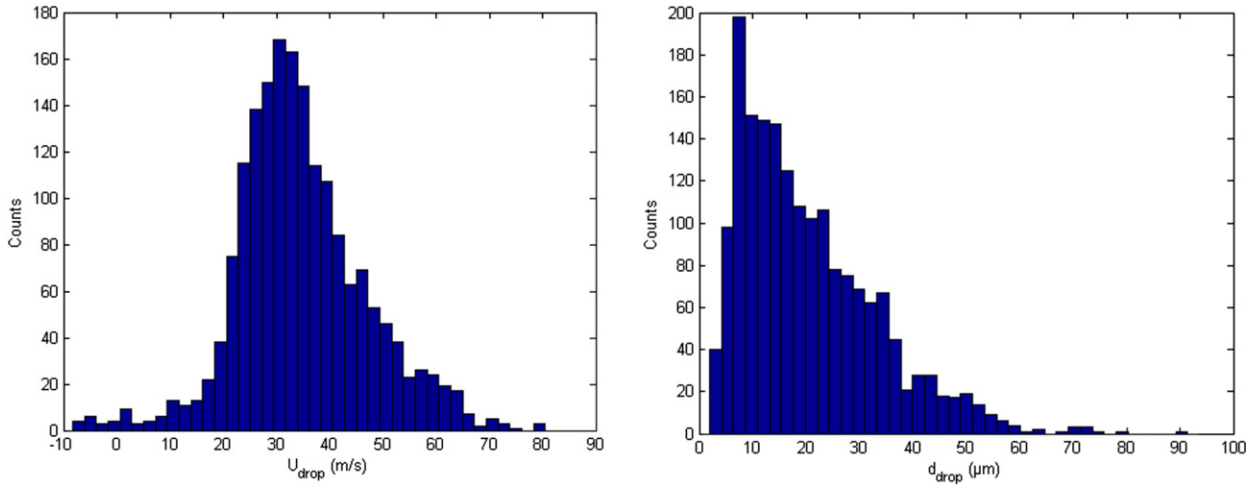

Average velocity: $U_{mean} = 34.7$ m/s
Standard deviation: $\sigma_u = 12.3$ m/s
Maximum velocity: $\max(U_{drop}) = 80.5$ m/s

Arithmetic mean diameter: $d_{10} = 20.4$ μm
Sauter mean diameter: $d_{32} = 36.1$ μm
Standard deviation: $\sigma_d = 12.8$ μm

Fig. 9. Velocity (left) and diameter (right) histograms for a run with $\Delta T_i = 87\,^{\circ}\mathrm{C}$ between 100 and 200 ms.

5. Results

5.1. Drop velocity and size distributions

Typical velocity and size distributions are shown in Fig. 9. It happens that their respective shapes do not evolve much when changing the superheat. The evolutions of various moments of these distributions (namely the arithmetic velocity average U_{mean}, the arithmetic mean diameter d_{10} and the Sauter mean diameter d_{32}) with the superheat are presented in Fig. 10: they will be discussed later. Note that, concerning the mean drop velocity, we do not attempt to correct for negative velocities. To gather more information out of these measurements, we also estimated the maximum velocity recorded as a tentative to assess the order of magnitude of the vapor velocity. From the joint size–velocity plot, it is clear that the largest velocities are obtained for thin drops, smaller than 5–10 μm. Hence, the latter may provide a reasonable estimate of the vapor velocity provided that the drops are not in an acceleration phase at the selected measuring location. Three methods have been used to estimate that maximum velocity. The first method consists in averaging the velocity data over the 5% fastest drops irrespective of their size. For the data of Fig. 9 (left), that concerns velocities above 58 m/s and the result is $U_{\max 5\%} = 63.2$ m/s. The second method consists in averaging the velocity of droplets with a diameter smaller that 5 μm and with a velocity above the mean velocity U_{mean}. This yields $U_{d<5\,\mu\mathrm{m}\,(U>U_{mean})} = 56$ m/s for the data of Fig. 9. The last estimate is performed by considering droplets with a diameter smaller that 10 μm and velocity larger than the mean. For the data of Fig. 9 that yields $U_{d<10\,\mu\mathrm{m}\,(U>U_{mean})} = 52.4$ m/s. Therefore, while the average drop velocity is about 30 m/s in Fig. 9, the maximum velocity happens to be much higher since it is comprised between 52 m/s and 63 m/s.

5.2. Evolution of drop characteristics with the superheat

Fig. 10 presents various average values of droplet velocity and size versus the initial superheat ΔT_i. The standard deviation is represented as an error bar for each condition. Data for the same initial superheats ($\pm 1\,^{\circ}\mathrm{C}$) have been accumulated to ensure the convergence.

The mean velocity increases with the initial superheat. That increase is slow between 10 °C and 40 °C and becomes much steeper and almost linear at higher superheats, i.e. for ΔT_i above about 40–50 °C. All the various averages velocities we defined exhibit the same trend. Note that the ratio between the maximum velocity and the mean velocity increases with the initial superheat: such a trend is consistent with an increasing vaporization rate and thus with larger vapor velocities as the thermodynamic disequilibrium growths.

Fig. 10 also shows that both the arithmetic mean and the Sauter mean diameters slightly decrease for an initial superheat between 10 °C and 40 °C, and then remain quasi-constant. Such a trend is not reported in the literature (cf. Introduction).

These evolutions may tentatively be related with a boiling front dynamics. Indeed, Reinke and Yadigaroglu [6] conducted experiments as the sudden depressurization of superheated liquids to atmospheric pressure. They observed the creation of a boiling front, which is a localized phase-change front where intense vaporization and fine-scale fragmentation occur at the interface. Although they do not provide any drop characteristics away from that front, they did measure the boiling front velocities. The latter were found to evolve almost linearly with the liquid superheat, which is an indication of how the

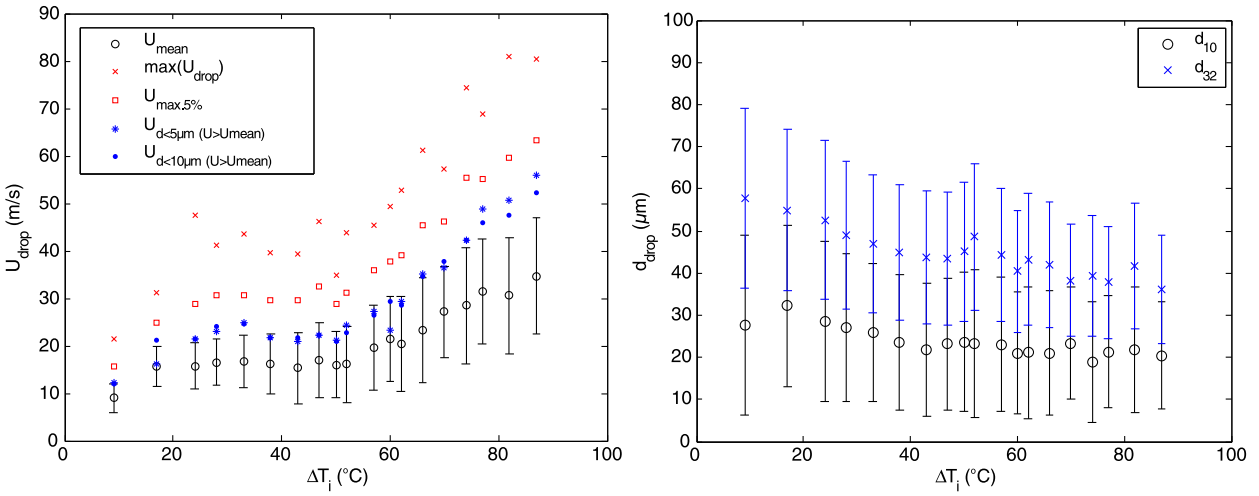

Fig. 10. Evolutions of average drop velocity and size with the initial superheat (fixed liquid flow rate: 0.27 kg/s). Bars correspond to standard deviations.

vapor flow rate evolves with the disequilibrium. In our case, we cannot visualize the presence of such a front (supposedly located near the valve). Moreover if it exists, it must be stationary (owing to the durations of our tests – some of them have being performed over many seconds). The common point is that the resulting vapor mass flow rate would linearly increase with the superheat, and, as it is that vapor flow that entrains droplets, the velocity of the latter is also expected to increase with the superheat. The plausibility of such a scenario is reinforced by the observed fact that the drop size distributions, and hence the droplet response time distributions, are not varying much with the disequilibrium. The last brick required in that scenario is the mechanism controlling the initial drop size. We can tentatively assume that the drop sizes are mainly controlled by the bursting at the liquid/vapor interface of the vapor bubbles, which are all located in the vicinity of the boiling front. According to the visualizations by Reinke and Yadigaroglu [6], the extend of the size distribution of these vapor bubbles are not too far from the standard deviation we measured on the droplets. Also vapor sizes were not evolving much with the superheat. The above atomization scenario clearly needs to be investigated further, but so far it seems compatible with a boiling front dynamics. If valid, it would also provide the initial conditions for the droplet ejection velocity (Duchemin et al. [7]).

As seen in that section, the PDI system provides reliable drop size and velocity distributions. Those evolutions with the superheat open new questions on the fundamental mechanics leading to the atomization. These data are also useful as input conditions for simulations.

5.3. Local volumetric flux and evaporation rate

The local volumetric flux of liquid as evaluated by the PDI (including probe volume corrections) is nearly constant, and happens to be quite low, around 0.25 cm/s. Even by correcting the flux according to the validation rate, the vaporized flow rate deduced by integrating the local flux over the tube cross-section is strongly overestimated. It is found that from 1.5% (at a superheat about 20 °C) to 3% (at a superheat about 90 °C) of the incoming liquid mass flow remains as liquid droplets. The proposed correction for the flux is therefore clearly insufficient, as we have seen that many droplets are actually missed by the PDI system.

Phase detection optical probes were therefore used to measure the local number density flux (see Hong et al. [8]). Contrary to the PDI, these sensors detect all the droplets hitting them, and provide a reliable estimate of the dispersed phase fraction.

Two probes (manufactured by A2PS company) were positioned just downstream the valve exit. Probe 1 was installed 7.5 mm from the valve center, at the opposite of the liquid entrance (Fig. 11). Probe 2 was used to scrutinize the distribution along a whole diameter (OJ axis in Fig. 11) using five different positions, spaced 5 mm from each other (see positions *a* to *e* in Fig. 11). The valve opening sequence was the same for each test: $\theta = 45°$, $\tau_o = 100$ ms, $\tau_p = \tau_c = 500$ ms (Fig. 2). The local number density flux φ_0 [#/m^2 s] is deduced from the mean drop detection frequency f_{detect} and from the mean drop cross-section area:

$$\varphi_0 = \frac{f_{detect}}{\pi \overline{R^2}}$$

The local volumetric flux, J_L [m/s] is then derived from φ_0 and from the mean drop volume, for uncorrelated size and velocity:

$$J_L = \frac{4}{3}\pi \overline{R^3}\varphi_0$$

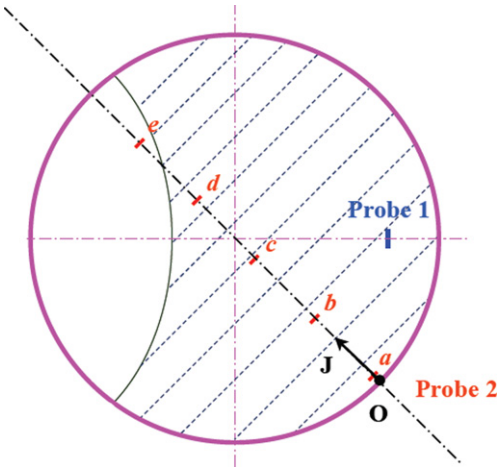

Fig. 11. Position of the two optical probes downstream the valve exit. The hatched area represents the ball valve for $\theta = 45°$.

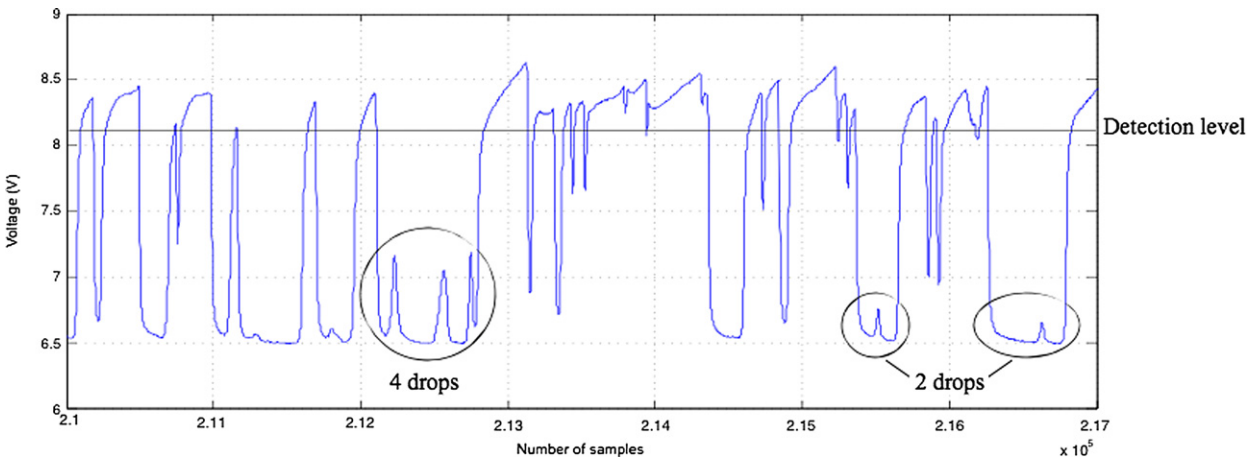

Fig. 12. Examples of multi-drops found for probe 2 in position a ($\Delta T_i = 58\,°C$, $Q_{m,\max} = 1.2$ kg/s).

In the above formula, the optical probes provide the detection frequency while the average area and volume are evaluated from PDI statistics. Assuming the local volumetric flux to be spatially uniform over the tube exit cross-section S, the global evaporation rate is then evaluated as:

$$F_{vap} = 1 - \frac{J_L S}{Q_{inj}}$$

where Q_{inj} is the incoming liquid volumetric flux deduced from $Q_{m,\max}$ and from the liquid density ($\rho_L = 1680$ kg/m^3). Note that the uniformity assumption is a severe approximation as the jets spread out over a 2π solid angle at the tube exit (see Fig. 4).

Several tests were conducted with probe 1 at different initial superheats and for two mass flow rates, namely $Q_{m,\max} = 1.2$ kg/s ($U_{inj} = 1.5$ m/s) and $Q_{m,\max} = 1.7$ kg/s ($U_{inj} = 2.1$ m/s). The mean detection frequency was evaluated over the entire signal record, i.e. including valve opening and closing phases. Only two initial superheats, 22 °C and 58 °C, were tested for probe 2 but for the five locations shown in Fig. 11. For that probe, the detection frequency was measured over the entire signal duration, t_{total}, and also over the plateau duration, $t_{plateau}$, where the regime is quasi-stationary. In addition, a correction was introduced to the flux by evaluating the fraction of drops missed by the signal processing. Indeed, in our conditions, some drops are so close to each other that the rising fronts of some signals are unable to reach the gas level (the upper voltage in Fig. 12): Fig. 12 shows examples of such multi-drop events. Current data processing detects a drop each time the signal amplitude becomes lower than the detection level set by the operator. If the probe dewetting is too slow, the rising edge does not cross the detection level before a new drop arrives on the probe and this creates multi-drops events: the later count for a single drop in the estimation of the detection frequency although 2 or more may have contributed to the signature.

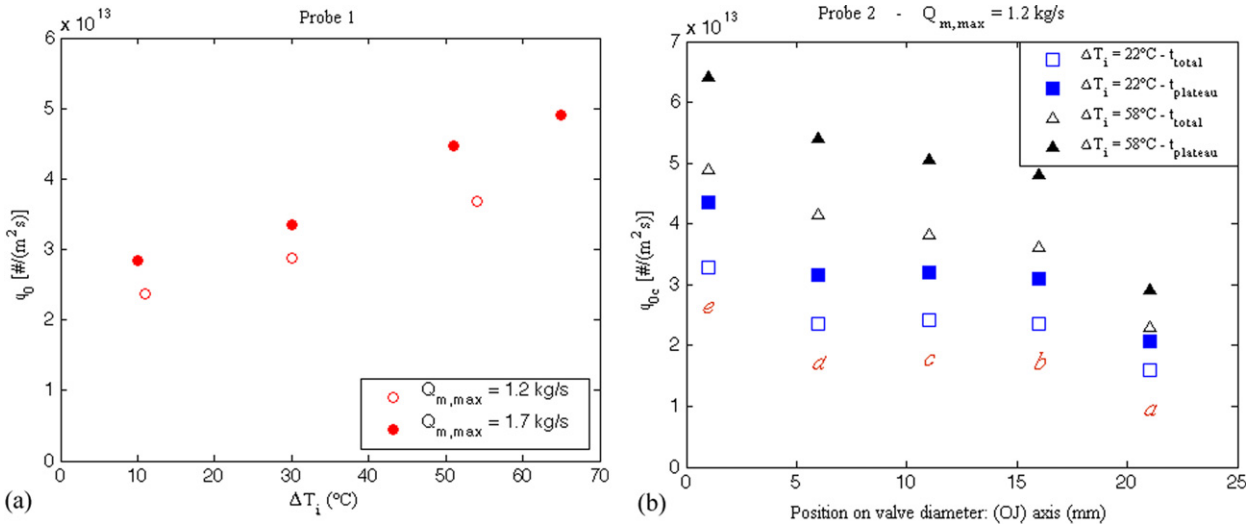

Fig. 13. (a) Local number density flux versus initial superheat for two injection flow rates (probe 1). (b) Corrected local volumetric flux profile over a diameter for two initial superheats (probe 2).

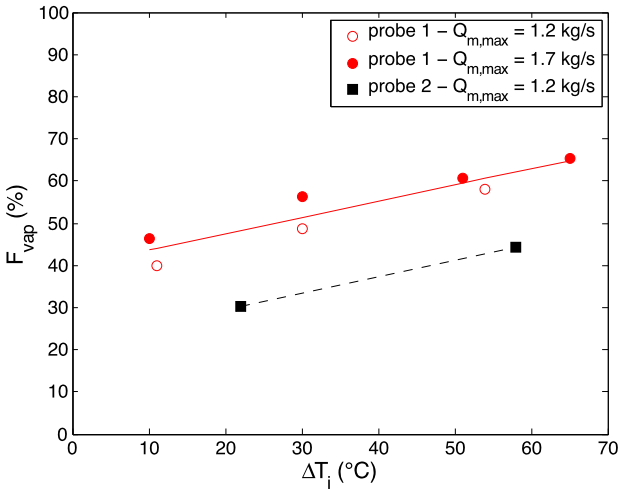

Fig. 14. Fraction of the incoming volumetric flux that evaporates versus initial superheat for the two optical probes.

From the manual analysis of a 4 ms record, we found that about 85% of the droplets are correctly detected whatever the initial superheat. The corrected local volumetric flux, φ_{0c}, is thus given by the measured value φ_0 divided by 85%. All the local flux measurements are presented in Fig. 13. A comparison can be made between probe 1 and probe 2 in position *e* with the measurements achieved over the whole duration t_{total}. The values provided by probe 1 happen to be slightly below those from probe 2 partly because they are not corrected for multi-drops events. The orders of magnitude are nevertheless quite close. The more reliable estimate is provided by the probe 2 exploited over t_{palier} and using the flux correction. The local number density flux happens to linearly increase with the initial superheat. It is also slightly increasing with the incoming liquid flow rate.

The global evaporation flux has been then deduced from these local measurements using an integration over the tube cross-section. For probe 2, the evaporation rate was deduced from a spatial average over the exit diameter of the corrected local number density flux evaluated on t_{palier}. The global evaporation flux scaled by the incoming flow rate is found to linearly but slowly increase with the initial superheat (Fig. 14). The slope is the same for both probes. Considering the results from probe 2, which are more reliable, the fraction of the incoming flux that evaporates varies from 30% (at a superheat about 20 °C) to 45% (at a superheat about 60 °C). That trend is fully consistent with global vaporization rate measurements deduced from the pressure time evolution in the vacuum tank.

Note that an alternate way to evaluate the evaporation rate is to reconstruct the vapor velocity at the exit from the tube from the drop velocities as measured at some distance downstream. For that, assumptions are needed on vapor velocity profiles and also on the initial drop ejection conditions. In addition, and without going into details, preliminary analysis

indicate that strong density gradients are to be expected in the gas phase in the near region downstream the valve, and that such gradients play a significant role on the droplet dynamics. As the density spatial distribution is not available from the present experiments, such an alternate method has not been considered.

6. Conclusion

Flashing experiments were conducted with FC-72 (C_6F_{14}) for superheats ranging from 5 °C to 90 °C. Visual observations with high-speed imaging have revealed a change in the jet angle when varying the initial superheat: for superheats above about 10 °C, the flashing is predominant and the jet opens at a 180° angle. Drop size and velocity measurements were performed with a PDI in these flashing regimes. This technique was adapted to these very dense conditions and careful parametric studies were conducted to test the validity of these measurements. The reliability of velocity and size distributions has been ascertained. However, by analyzing the data rate, it was also shown that many droplets escape detection and hence that the volumetric flow is strongly underestimated. To circumvent this limitation, phase detection optical probes were used to measure the mean drop detection frequency. Combining the drop average area and volume deduced from PDI measurement and such detection frequencies, we were able to access to the local number density flux and also to estimate the global evaporation flux. The later was found to linearly increase with the initial superheat, a result fully consistent with global vaporization rate measurements based on the pressure growth in the tank.

From experiments performed at a fixed liquid flow rate, and for initial superheats above 40 °C, the mean drop velocity was found to quasi-linearly increase with the initial superheat while both the arithmetic and the Sauter mean diameters remained constant. These behaviors, in particular for the drop size, markedly differ from the few available results for depressurization through a small orifice. Yet, these trends are compatible with a regime consisting of a localized boiling front as described notably by Reinke and Yadigaroglu [6]. A plausible scenario for the drop formation is proposed that may help understanding how the atomization occurs during flashing. The data presented provide also useful information for numerical simulations.

References

[1] R. Brown, J.L. York, Sprays formed by flashing liquid jets, AIChE J. 8 (1962) 149–153.
[2] E. Hervieu, T. Veneau, Experimental determination of the droplet size and velocity distributions at the exit of the bottom discharge pipe of a liquefied propane storage tank during a sudden blowdown, J. Loss Prev. Process Ind. 9 (1996) 413–425.
[3] D. Yildiz, P. Rambaud, J. Van Beeck, J.M. Buchlin, Evolution of the spray characteristics in superheated liquid atomization in function of initial flow conditions, in: ICLASS, Kyoto, Japan, August 27–September 1, 2006.
[4] R. Lecourt, P. Barricau, J. Steelant, Spray velocity and drop size measurements in flashing conditions, At. Sprays 19 (2009) 103–133.
[5] A. Naqwi, R. Menon, A rigorous procedure for design and response determination of phase Doppler systems, in: R.J. Adrian, D.F.G. Durao, F. Durst, M.V. Heitor, M. Maeda, J. Whitelaw (Eds.), Developments in Laser Techniques and Applications to Fluid Mechanics, Proceedings of the 7th International Symposium, Lisbon, Portugal, 11–14 July, Springer, 1994.
[6] P. Reinke, G. Yadigaroglu, Explosive vaporization of superheated liquids by boiling fronts, Int. J. Multiphase Flow 27 (2001) 1487–1516.
[7] L. Duchemin, S. Popinet, C. Josserand, S. Zaleski, Jet formation in gas bubbles bursting at a free surface, Phys. Fluids 14 (2002) 3000–3008.
[8] M. Hong, A. Cartellier, E.J. Hopfinger, Characterization of phase detection optical probes for the measurement of the dispersed phase parameters in sprays, Int. J. Multiphase Flow 30 (2004) 615–648.